JOURNAL OF GEOPHYSICAL RESEARCH, VOL. , XXXX, DOI:10.1029/,

# Helicity of magnetic clouds and their associated active regions

Robert J. Leamon,[1] Richard C. Canfield, Sarah L. Jones,[2] Keith Lambkin,[3]

Brian J. Lundberg,[4] and Alexei A. Pevtsov[5]

Department of Physics, Montana State University

---

R. C. Canfield and R. J. Leamon, Department of Physics, Montana State University, Bozeman, MT 59717-3840. (email: canfield@physics.montana.edu, leamon@physics.montana.edu)

S. L. Jones, Department of Physics and Astronomy, Dartmouth College, Hanover, NH 03755. (email: Sarah.L.Jones@dartmouth.edu)

K. Lambkin, Experimental Physics Department, University College Dublin, Dublin 4, Republic of Ireland. (email: keithlambkin@hotmail.com)

B. J. Lundberg, Department of Physics, The University of Arizona, Tucson, AZ 85721. (email: lundberg@email.arizona.edu)

A. A. Pevtsov, National Solar Observatory, Sunspot, NM 88349. (email: apevtsov@nso.edu)

[1]EER Systems at GSFC

[2]Dartmouth College

[3]University College Dublin

[4]The University of Arizona

[5]National Solar Observatory

**Abstract.** In this work we relate the magnetic and topological parameters of twelve interplanetary magnetic clouds to associated solar active regions. We use a cylindrically symmetric constant-$\alpha$ force-free model to derive field line twist, total current, and total magnetic flux from in situ observations of magnetic clouds. We compare these properties with those of the associated solar active regions, which we infer from solar vector magnetograms.

Our comparison of fluxes and currents reveals: (1) the total flux ratios $\Phi_{MC}/\Phi_{AR}$ tend to be of order unity; (2) the total current ratios $I_{MC}/I_{AR}$ are orders of magnitude smaller; and (3) there is a statistically significant proportionality between them. Our key findings in comparing total twists $\alpha L$ are: (1) the values of $(\alpha L)_{MC}$ are typically an order of magnitude greater than those of $(\alpha L)_{AR}$; and (2) there is no statistically significant sign or amplitude relationship between them. These findings compel us to believe that magnetic clouds associated with active region eruptions are formed by magnetic reconnection between these regions and their larger-scale surroundings, rather than simple eruption of pre-existing structures in the corona or chromosphere.

## 1. Introduction

Coronal mass ejections (CMEs) are an almost daily occurrence on the sun. Interplanetary manifestations of CMEs often have a very distinct magnetic structure, namely a large-scale helix. *Burlaga et al.* [1981] described this magnetic structure as a "Magnetic Cloud." According to Burlaga's definition, three properties are required to identify a structure as a magnetic cloud: (*i*) a very low proton temperature; (*ii*) a large, smooth, monotonic rotation of the field direction; and (*iii*) enhanced magnetic field strength. The general case of a smooth, monotonic rotation of the field direction is called a magnetic flux rope. At least one-third [*Gosling*, 1990], and, according to some researchers [*e.g.*, *Lepping and Berdichevsky*, 2000; *Webb*, 2000] considerably more, of the interplanetary manifestations of CMEs observed *in situ* have magnetic flux rope (large-scale helix) structure.

There exist two basic ideas about the solar origins of the topology of magnetic clouds. Some investigators [*e.g.*, *Crooker*, 2000; *Mulligan et al.*, 2000] view solar eruptions as global, i.e., defined by the overall dipolar magnetic field of the Sun. In this view, the field lines of the helmet streamer belt become the outermost coils of the magnetic cloud through reconnection behind the CME as it lifts off [*e.g.*, *Gosling*, 1990; *Crooker et al.*, 1998]. Hence the leading field direction of magnetic clouds tends to follow that of the large-scale solar dipole, reversing at solar maximum. On the other hand, other authors studying filament eruptions [*e.g.*, *Bothmer and Rust*, 1997; *Bothmer and Schwenn*, 1998] view them as local events, with interplanetary magnetic field (IMF) orientations correlating with the solar dipole only because the toroidal fields in filaments do so. Such a local viewpoint has also been taken in the "breakout" model of active region eruptions [*Antiochos*, 1998;

*Antiochos et al.*, 1999]: the topology of the active region determines that of the magnetic cloud [*Lynch et al.*, 2002].

The relationship between magnetic clouds and their solar progenitors may be much more straightforward for filaments [*Bothmer and Rust*, 1997; *Crooker*, 2000] than active regions [*Pevtsov and Canfield*, 2001; *Leamon et al.*, 2002]. However, a large fraction of CMEs are associated with solar active regions. Using images from both the LASCO [*Brueckner et al.*, 1995] and EIT [*Delaboudinière et al.*, 1995] instruments on the SOHO mission [*Domingo et al.*, 1995], *Subramanian and Dere* [2001] found that of the 32 CME-related transients in their study, 41% were associated with active regions without prominence eruptions, 44% were associated with eruptions of prominences embedded in active regions, and only 15% were associated with eruptions of prominences outside active regions. Those CMEs that did not involve prominence eruptions originated in active regions both with and without prominences. It seems likely that a comprehensive understanding of the relationship between interplanetary disturbances and their progenitor solar regions should be based on a broad view that considers the magnetic structure of both prominences and active regions. However, from the observational point of view, the available data and associated analysis techniques are quite different for these two phenomena. In particular, vector magnetic field measurements are available only for active regions. Hence, in this work we have chosen to concentrate on magnetic cloud events associated with active regions.

This research is motivated by results that *Luhmann et al.* [2002] have obtained on combinations of active region and large scale fields that are sensitive to reconfiguration by eruption. They conclude that CMEs occur in conjunction with certain helmet streamer configurations where the streamer is sensitive to the involved active region, which has

nonpotential character. As well, it is motivated independently by results that we [*Leamon et al.*, 2002] have obtained on the relationship between solar and interplanetary phenomena, discussed below. From these studies, we are led to explore the interaction between active regions and the large-scale field as a factor in solar eruptions and the formation of magnetic clouds.

*Leamon et al.* [2002] studied a set of 46 solar coronal eruptions associated with the eruption of X-ray sigmoids, which are known to be productive of such events [*Canfield et al.*, 1999]. In the large-scale dipole model [*e.g.*, *Crooker*, 2000, her Figure 6]. the arcade of field lines whose apex marks the base of the heliospheric current sheet becomes the outermost coil of the magnetic cloud, as discussed above. In contrast, in active-region flux rope models the field lines of the CME-associated active region, already of flux-rope form before the eruption starts, are assumed to expand in a self-similar manner, so the outermost field lines of the flux rope become the leading edge of the magnetic cloud [*Titov and Démoulin*, 1999, their Figure 2]. *Leamon et al.* [2002] showed that in their dataset neither the large-scale dipole model nor the active-region flux rope model is significantly better than the toss of a coin in predicting the relationship between individual magnetic clouds and their progenitor solar magnetic fields.

In section 2 we describe our data sources and analysis techniques for magnetic clouds and active regions. We then compare our solar and interplanetary results in section 3, focusing separately on fluxes and currents in section 3.1 and field line twist in section 3.2. In section 4 we show that both considerations lead us to a picture in which reconnection of the active region with its surroundings plays a central role.

## 2. Observations and Data Analysis

We use data from the following missions/ instruments for this study: Yohkoh/SXT [*Tsuneta et al.*, 1991]; WIND/MAG [*Lepping et al.*, 1995] and SWE (thermal plasma) [*Ogilvie et al.*, 1995]; SOHO/MDI [*Scherrer et al.*, 1995]; and the Haleakala Stokes Polarimeter (Mees Solar Observatory, Hawai'i) [*Mickey*, 1985]. The SOHO/LASCO coronagraph [*Brueckner et al.*, 1995] was also used qualitatively for event identification purposes.

We limit our search for events to the overlap between the Yohkoh and WIND missions. Time coverage of *in situ* data from OMNI (ISEE-3/ IMP-8) before this time is sporadic; while there is enough data to identify the existence of a cloud, sufficient coverage for a multi-parameter least-squares fit is a more stringent demand on the data. While we do not require data from the SOHO mission, having LASCO and MDI data did make selection and analysis easier, and the final dataset does show a bias towards the overlap of all three spacecraft. We need to unambiguously identify the solar source of each magnetic cloud to be able to compare quantities such as current, flux and twist. As a first filter, we look at the LASCO list for halo or partial halo CMEs occurring at about the right time, as calculated the constant velocity transit time (147 million km divided by the average solar wind speed observed in the interplanetary ejecta), and exclude events where there are two (or more) possible sources that erupted within less than a day of one another. We search the SXT archive for corresponding signs of flaring, brightening or eruption and identify the active region, if any; quiet-sun events are discarded. We delete any events for which there is evidence that CME interaction plays a role [*Gopalswamy et al.*, 2002].

Finally, we check the HSP archive for vector magnetogram data for said AR near the times of eruption, and discard any events without magnetograms. The non-existence of

HSP data was the most limiting filter in eliminating possible events for study, especially around solar maximum. Since we know that active regions, as a whole, evolve on time scales of days, we accept time differences of up to about two days. When all is said and done, we have only 12 events to study. However, as we shall show below, this number is sufficient to yield a statistically significant result.

### 2.1. Interplanetary Data Analysis and Results

Following *Lepping et al.* [1990], we model magnetic clouds using the constant-$\alpha$ force-free field solution of *Lundquist* [1950], which assumes cylindrical symmetry. Since this work is an exploration of the relationship of the helicity of magnetic clouds to that of solar active regions, which are represented by constant-$\alpha$ force-free models [*Pevtsov et al.*, 1995], the simple cylindrical constant-$\alpha$ force-free flux rope model is ideal.

Details of our magnetic cloud model and code are described in Appendix A. As an example of its application, Figure 1 shows a magnetic cloud from August 12–13, 2000, resulting from a CME associated with AR 9114 on August 9. The vertical dashed lines delineate the cloud boundaries; inside, the rotation of the magnetic field from north to south, with a steady eastwards component, is easily seen. The north to east to south rotation is indicative of a right-handed flux rope. Overlaid are the best-fit curves from the constant-$\alpha$ force-free field mode; the axis of the flux rope is inclined at 11° below the ecliptic plane, and is 82° from the Earth-Sun line (*i.e.*, pointing not quite due east).

**Appendix**

**Figure 1**

Table 1 shows the properties of the 12 magnetic cloud events observed in the solar wind at 1 AU. Columns 5–9 show the best-fit parameters $\theta_0$, $\phi_0$, $B_0$, $R_0$ and $H$ as determined from our Downhill-Simplex code. The tenth column is a dimensionless measure of the goodness-of-fit, the minimum $\chi^2$ error of the best fit, normalized by the axial magnetic

**Table 1**

field. *Lepping et al.* [1990] found their best fit by minimizing $\chi^2$; instead, we minimize $\chi^2$ and then scale by the fit parameter $B_0$. We found that using *Lepping et al.*'s method leads to undue statistical weight being placed on finding solutions with large $B_0$, frequently coupled with radii of several AU and high impact parameters. These solutions were dismissed as clearly not physically sensible. Finally, we have the current $I_{MC}$ and the magnetic flux $\Phi_{MC}$, as defined below, and the force-free parameter $\alpha$, as defined by equation (A2).

The total current $I$ flowing in the flux rope can be calculated

$$I = \int \mathbf{J} \cdot d\mathbf{A} = \int \left( \frac{\alpha \mathbf{B}}{\mu_0} \right) \cdot d\mathbf{A}. \tag{1}$$

We may consider the axial and azimuthal components of equation (1) separately (from equation (A1), there is no radial component of the magnetic field and thus no radial current density). The axial current depends only on the axial component of the magnetic field, which varies as the zeroth-order Bessel function. With cylindrical symmetry $dA = 2\pi r\, dr$ and simple integration then gives

$$I_{MC} = 2\pi(0.51915){\mu_0}^{-1} B_0 R_0 \tag{2}$$

where the numerical factor, resulting from the limits of integration, is $J_1(2.4048)$. Note that the current is indirectly dependent on $\alpha$.

By a similar integral to equation (1), the magnetic flux $\Phi$ in the flux rope is:

$$\Phi_{MC} = 2\pi(0.21588) B_0 R_0^2. \tag{3}$$

The average radius of the 12 clouds in Table 1 is 24.3 million km, or 0.16 AU. The average twist per unit length $\langle \alpha \rangle = 1.24 \times 10^{-10}$ m$^{-1}$, or 18 AU$^{-1}$. The average axial magnetic field strength is 18 nT. Combining the field strength and radius by equations (2)

and (3) gives $\langle I_{MC} \rangle = 1.13 \times 10^9$ A, and $\langle \Phi_{MC} \rangle = 16.1 \times 10^{12}$ Wb. In the cgs system of units, 1 Wb = $10^8$ Mx. The mean cloud axis lies in the ecliptic plane ($\langle \theta_0 \rangle = 6^\circ \pm 8^\circ$), and the mean absolute elevation from the ecliptic plane is 22°. The average azimuth from the GSE $x$-direction is 162°; however, if we take the direction modulo 180 (ignoring the direction of pointing), the average azimuth lies close to right angles to the earth-sun line at $103^\circ \pm 12^\circ$. The above results are in general agreement with previous works cataloging magnetic clouds [*e.g.*, *Lepping et al.*, 1990; *Lepping et al.*, 1997; *Mulligan et al.*, 1998]. Appendix B discusses discrepancies between various authors' fits to one particularly well-analyzed magnetic cloud event, in a quantitative manner.

### 2.2. Solar Data Analysis and Results

We seek to compare the values of total current, total flux, and overall twist density (measured by the force-free-field parameter $\alpha$) in magnetic clouds to the values of the same quantities inferred from vector magnetograms of their associated solar active regions. Table 2 summarizes our solar active region data and results. Columns 2 and 3 define the date and time of the eruptive event (except where obelised, from Yohkoh/SXT) and column 4 the start time of the vector magnetogram scan. Note that for some events, we have multiple magnetograms, frequently before and after the eruption. Unavoidable uncertainty is present in the analysis for those cases in which the magnetogram times are more than a day or two from the eruption times.

**Table 2**

The HSP routinely makes active region vector magnetograms using the Stokes profiles of the Zeeman-sensitive Fe I $\lambda\lambda$6301.5, 6302.5Å doublet, rastering over a rectangular area that is typically a few arc minutes on each side (2.8 arc minutes in the example in Figure 2). At each raster point the strength of the longitudinal ($B_L$) and transverse ($B_T$)

**Figure 2**

components of the field (relative to the line of sight), and the azimuth $\phi$ of the transverse field, are shown through the use of contours and line segments. These values are determined from the Stokes profiles using the non-linear least-squares inversion technique of *Skumanich and Lites* [1987], which takes into account magneto-optic effects (*e.g.*, Faraday rotation) and magnetic filling factor. We resolve the 180° ambiguity in $\phi$ and transform the magnetogram to heliographic coordinates, in which the magnetic field is described by the vertical component $B_z$ and horizontal components $B_x$ and $B_y$. The vertical current density $J_z$ is then derived using Ampère's Law,

$$\frac{4\pi}{c} J_z = (\nabla \times \mathbf{B}) \cdot \hat{\mathbf{z}} = \frac{\partial B_y}{\partial x} - \frac{\partial B_x}{\partial y}. \tag{4}$$

*Canfield et al.* [1993] explain these procedures in detail.

We first identify, in the vector magnetogram, the boundaries of the area that contains the photospheric footpoints of the active region flux system, *i.e.*, those magnetogram pixels that lie at the footpoints of the coronal active region loops seen by Yohkoh SXT. For this purpose we use easily co-registered overlays of SXT images and MDI magnetograms, as in the example shown in the left panel of Figure 2. We use these overlays to draw the flux system boundary on the corresponding HSP magnetogram (right panel). We do not need to co-register the MDI and HSP magnetograms; it is a simple exercise in pattern recognition to use the $B_L$ contours in both the left and right panels of Figure 2 to draw the flux system boundary on the vector magnetogram. Moreover, it is not necessary to draw this boundary precisely; because it falls outside the strong-flux area of the magnetogram, the derived total currents and fluxes are insensitive to plausible variations in its location. The boundary is used for two purposes. We use the region outside it to determine the noise levels by computing the standard deviations $\sigma(B_L)$ and $\sigma(B_T)$ of the histograms of $B_L$

and $B_T$ values. The average value of $\sigma(B_L)$ in the vector magnetograms used in this study is 20 G and the average value of $\sigma(B_T)$ is 70 G. We use the region inside the boundary to determine the values of $I_{AR}$ and $\Phi_{AR}$ given in columns 6 and 7 of Table 2. $I_{AR}$ and $\Phi_{AR}$ are the total unsigned current and magnetic flux respectively, *i.e.*, $I_{AR} = \sum_i |J_z(i)| S_p/2$ and $\Phi_{AR} = \sum_i |B_z(i)| S_p/2$ over all pixels inside the boundary, where $S_p$ is the HSP magnetogram pixel area.

Because of the influence of noise, $I_{AR}$ and $\Phi_{AR}$ are upper limits to plausible values within the active region boundaries. We derive corresponding lower limits by including in the sums only those pixels whose $B_T$ values exceed 300 Gauss. Typically these values, hereafter denoted $I_{AR}^{300}$ and $\Phi_{AR}^{300}$, are roughly half the upper limits. These values of the upper and lower limits define the ranges given in columns 6 and 7 of Table 2. They vary widely, but the averages ($\sim 30 - 50$ TWb respectively) are somewhat greater than the median value ($\sim 25$ TWb) of the distribution given by *Howard* [1989].

We determine a dipole length scale $\ell$ for each active region by determining the flux-weighted centroids of all positive and negative flux. We include in that determination all pixels inside the boundary that meet the criterion that ${B_L}^2 + {B_T}^2 > 4\,(\sigma^2(B_L) + \sigma^2(B_T))$. The values of $\ell$ appear in column 8 of Table 2. The tilt of the line between the two centroids with respect to the solar equator is given in the last column of this table.

We measure the overall twist of the active region magnetic field following *Pevtsov et al.* [1995], who introduced $\alpha_{\rm best}$, the value of $\alpha$ for a linear force-free field $\nabla \times \mathbf{B} = \alpha \mathbf{B}$ that gives the best least-squares fit to the observed $B_x$ and $B_y$ field in a vector magnetogram, constrained by the observed $B_z$ distribution. *Leka* [1999] and *Burnette et al.* [2004] found that this measure is quantitatively robust when proper attention is paid to noise. Values

of $\alpha_{AR}$ determined in this manner, using only pixels whose measured $B_T$ values exceed 300 G (over three times the noise level) are given in the penultimate column of Table 2.

## 3. Discussion: Solar–Interplanetary Comparisons

Using the methods discussed above, we have analyzed both interplanetary and solar data to determine values of total current, total magnetic flux, and the force-free-field parameter $\alpha$ in magnetic clouds and associated active regions. We consider the relationship between these quantities in terms of what we believe to be a valid first approximation to the expansion of interplanetary magnetic clouds: the sub-Alfvenic hydromagnetic expansion of a force-free highly-ionized plasma. In this approximation, both the total flux and the total current in an expanding cloud are conserved quantities, since the current density is simply proportional to $B$, and the magnetic field is frozen into the plasma.

### 3.1. Fluxes and Currents

There are several noteworthy features in the relationship between magnetic flux and electric current values in MCs and ARs, which are shown in the sixth and seventh columns of Table 3. These features can be discussed in the framework of three highly simplified, but conceptually useful, models of the solar genesis of magnetic clouds. These models are that the flux in the magnetic cloud originates in: (1) the active region alone (the AR model); (2) the overlying large-scale dipole alone (the LSD model); (3) a region of reconnection of the active region and the large-scale dipole (the AR-LSD reconnection model).

**Table 3**

First, the flux ratios $\Phi_{MC}/\Phi_{AR}$ seen in Table 3 tend to be large. In three events (Nos. 3, 9, and 11) listed in Table 3, observed values of the flux ratio greater than 100% are listed,

but only event No. 3 exceeds 100% of the flux value before the eruption. This latter event is thus inconsistent with the AR model, but consistent with the LSD model, which has no upper limit on the ratio, and the AR-LSD reconnection model, whose upper limit is 200%. This is but a single case, so we conclude that the large flux ratios do not pose an obvious problem.

Studies by *Webb et al.* [2000b] and *Lepping et al.* [1997] have used a different approach from ours, in which specific boundaries of the solar source region are inferred from images (EIT, SXT, H$\alpha$). After identifying dimming regions or plausible footpoints of erupting filaments as the solar source regions, they use MDI magnetograms to infer the associated flux $\Phi_{SUN}$, as distinct from our $\Phi_{AR}$, which measures the flux of the whole active region and none of nearby quiet areas. *Webb et al.* [2000b] estimated $\Phi_{SUN}$ associated with the well-observed May 1997 event from the dimming regions of an EIT 195Å image. Their source region included much of the flux of the active region, but did not extend substantially beyond it. They determined $\Phi_{MC}/\Phi_{SUN}$ to be 73%. *Lepping et al.* [1997] studied the relationship of $\Phi_{MC}$ to the $\Phi_{SUN}$ using EIT, SXT, and H$\alpha$ observations. They studied three disappearing-filament events, which appear to involve much more flux outside the related active regions than the event studied by *Webb et al.* [2000b], and concluded that $\Phi_{MC}/\Phi_{SUN} \sim 250\%$. Because $\Phi_{SUN}$ is conceptually different from our $\Phi_{AR}$, our results and theirs cannot be compared directly. However, their results seem consistent with our finding that the flux ratios $\Phi_{MC}/\Phi_{AR}$ tend to be large.

Second, the current ratios $I_{MC}/I_{AR}$ seen in Table 3 tend to be orders of magnitude less than the flux ratios $\Phi_{MC}/\Phi_{AR}$. This makes sense only in the context of the AR and AR-LSD reconnection models, if there is no significant current present outside the cores of

active regions. Although this view is reasonable, it is hard to defend, since as a practical matter vector magnetographs lack sufficient sensitivity to measure currents beyond the strong-field areas of active regions. It remains possible that there exist on the Sun very extended regions outside ARs with current density that is low, but nevertheless not so low that their contribution to the total current of MCs is negligible.

The third feature of the results in Table 3 is that there is a statistically significant proportionality between the flux ratios $\Phi_{MC}/\Phi_{AR}$ and the current ratios $I_{MC}/I_{AR}$. This result is expressed in graphical form in Figure 3, which shows that as the flux ratio grows, so does the current ratio. This is expressed in the figure as linear trend, which has a slope of $1.15 \pm 0.16 \times 10^3$. Whether or not the relationship is linear, it is demonstrably real, as evidenced by a Spearman rank-order correlation coefficient of 0.811, with confidence level 99.8%. This trend can most easily be explained in terms of the AR-LSD reconnection model, in which half of the flux of the MC originates in the outer shell of the active region, and as more of the AR flux goes into the MC, so does the associated AR current. There is no reason whatsoever to expect this trend in the LSD model. In the AR model, one might think that it would arise if ARs with more current in proportion to their flux (larger $\alpha$, more free energy) tended to be more eruptive. However, the combination of $I_{MC} \ll I_{AR}$ and $\Phi_{MC} \sim \Phi_{AR}$ argues against this model, since one cannot plausibly take essentially all the flux of an active region without taking with it more than a tiny fraction of the current.

**Figure 3**

### 3.2. Twist

Since $\alpha$ is a twist density, the product $\alpha L$ is a measure of the overall twist contained in length $L$. To determine $\alpha L$ for active regions, we have inferred $L$ values from the

vector magnetograms by adopting the approximation that the coronal AR field lines are semicircular, so $L = \pi\ell/2$. For magnetic clouds, on the other hand, $L$ is the length of the axis of the flux rope arcing from the base of the corona to 1 AU and back. To the best of our knowledge, the only work to directly measure this length and number of turns $N_{\rm turns}$ in an interplanetary flux rope is *Larson et al.* [1997], who used solar flare electron time-of-flight arguments to show that the October 18–20, 1995 event had 4 turns between the flare site and 1 AU. This unique observation allows us to test our methods for using $\alpha L$ to estimate $N_{\rm turns}$. *Larson et al.* [1997] determined that the cloud's radius is 0.14 AU, so $\alpha \simeq 17$ AU$^{-1}$, and their calculated length of a field line close to the cloud axis was 2.5 AU. Thus $N_{\rm turns} = \alpha L/(2\pi) = 6.8$, in reasonable agreement with their observed value of 8.

The measurement of *Larson et al.* [1997] is unique, but we can use straightforward assumptions to justify use of their value of $L = 2.5$ AU as a first approximation for all clouds. If a magnetic cloud were to be a perfect toroid extending from Sun to Earth by the time it encounters a spacecraft close to Earth, it would have $L = 3.14$ AU; at the other extreme, a "needle" magnetic cloud (however implausible) would have $L = 2$ AU. Splitting the difference we have the *Larson et al.* $L = 2.5$ AU result, which we have used in computing the magnetic cloud $(\alpha L)_{MC}$ values in column 9.

The values of $(\alpha L)_{AR}$ and $(\alpha L)_{MC}$ given in the last two columns of Table 3 show two noteworthy properties. First, the values of $(\alpha L)_{MC}$ are typically an order of magnitude greater than those of $(\alpha L)_{AR}$. Second, there is no systematic sign or amplitude relationship between them. In only 8 of 12 events do the signs agree; it is thus hardly surprising that we find the Spearman rank-order correlation coefficient is 0.04 and the confidence level

is only 10%, *i.e.*, there is no statistically significant relationship. This lack of correlation is in agreement with *Leamon et al.* [2002], who showed that a magnetic cloud could not simply be a sigmoid expanding out of the solar atmosphere, however such structures are explained. It is also in agreement with our finding that the Spearman rank-order correlation coefficient between the tilt of active regions and the latitude (tilt w.r.t. the ecliptic) of the cloud axes is $-0.255$, but the confidence level of is only 73%, implying no real statistical significance.

These two properties—that the values of $(\alpha L)_{MC}$ are typically an order of magnitude greater than those of $(\alpha L)_{AR}$, and that there is no systematic sign or amplitude relationship between them—can also usefully be discussed in the context of the three simple models introduced at the start of section 3.1. Clearly the fact that the values of $(\alpha L)_{AR}$ are an order of magnitude less than those of $(\alpha L)_{MC}$ immediately rules out models in which a magnetic cloud is formed by a coronal structure simply lifting off into space, namely the AR model. Similarly, it rules out models in which the magnetic cloud is formed without reconnection from the large-scale corona, for which there is no evidence of highly twisted fields. We are compelled to believe that only models that invoke magnetic reconnection in the eruptive process can produce so many turns within the resulting magnetic cloud. It is noteworthy that such reconnection models can also readily explain the lack of relationship between $(\alpha L)_{AR}$ and $(\alpha L)_{MC}$. *Zhang and Low* [2003] show that magnetic reconnection can readily reverse the twist direction of a flux rope emerging into pre-existing fields, due to interplay between the internal magnetic helicities of the two flux systems and their mutual magnetic helicity.

## 4. Summary

In the preceding section we have discussed our results in terms of three simple models—that flux in magnetic clouds originates in: (1) active regions (the AR model); (2) the overlying large-scale dipole (the LSD model); (3) a region that has experienced reconnection of the active region and the large-scale dipole (the AR-LSD reconnection model). The upshot of our consideration of the large flux ratios $\Phi_{MC}/\Phi_{AR}$, the fact that the flux ratios $\Phi_{MC}/\Phi_{AR}$ tend to be much larger than the current ratios $I_{MC}/I_{AR}$ and the statistically significant proportionality between the flux ratios $\Phi_{MC}/\Phi_{AR}$ and the current ratios $I_{MC}/I_{AR}$ is that only the reconnection model (3) emerges unscathed. As well, the reconnection model is the only one that can explain that the values of $(\alpha L)_{MC}$ are typically an order of magnitude greater than those of $(\alpha L)_{AR}$ and that there is no systematic sign or amplitude relationship between them. Hence, we are compelled to believe that only models that invoke magnetic reconnection between active regions and their large-scale overlying fields in the eruptive process can explain the relationships between total flux, total current, and associated twist of magnetic fields of active regions and associated magnetic clouds revealed in this study.

## Appendix A: Magnetic Cloud Model

We follow *Lepping et al.* [1990], using the constant-$\alpha$ force-free field solution of *Lundquist* [1950] and cylindrical geometry. For constant $\alpha$, $\nabla \times \mathbf{B} = \alpha\mathbf{B} = \mu_0\mathbf{J}$ becomes $\nabla^2\mathbf{B} = -\alpha^2\mathbf{B}$, since $\mathbf{B}$ is divergence-free. The solutions in cylindrical coordinates given

by *Lundquist* [1950] are:

$$\left.\begin{aligned} B_A &= B_0 J_0(\alpha r) \\ B_T &= H B_0 J_1(\alpha r) \\ B_R &= 0. \end{aligned}\right\} \tag{A1}$$

where $B_A$, $B_T$ and $B_R$ are, respectively, the axial, tangential (azimuthal) and radial components of the magnetic field; $B_0$ is the field strength on the axis of the cylinder; $H = \pm 1$ is the handedness of the flux rope ($+1$ for right-handed, $-1$ for left-handed); and the $J_n$ are the $n$th order Bessel functions. The force-free parameter $\alpha$ is related to the size of the cloud by

$$\alpha = 2.4048/R_0, \tag{A2}$$

where the numerical factor is the location of the first zero of $J_0$.

After rotating from cloud-centered coordinates to the GSE coordinate system, the model ($\mathbf{B}^M$) is the least-squares best fit to the observed data ($\mathbf{B}$), minimizing

$$\chi^2 = \frac{1}{3N} \sum \left[ (B_x - B_x^M)^2 + (B_y - B_y^M)^2 + (B_z - B_z^M)^2 \right] \tag{A3}$$

by means of the downhill-simplex method of *Nelder and Mead* [1965]. The factor $3N$ enters from the 3 magnetic field components for each of $N$ hourly averaged observed data points used. We use the routine "`amoeba`" as given in section 10.4 of *Press et al.* [1992]. The least-squares analysis returns the following parameters, as variables in the model: (*i*) $\theta_0$ and $\phi_0$, the latitude and longitude, respectively, of the cloud's axis; (*ii*) $R_0$, the radius of the cloud; (*iii*) $Y_0$, the impact parameter, or distance of the spacecraft from the cloud axis at closest approach. Unlike previous models of magnetic clouds, we do not fit the cloud handedness $H = \pm 1$. Instead, the handedness is determined from visual inspection of the time-series data and entered into the model as a fixed parameter.

As the downhill-simplex method can converge on local minima, rather than the global minimum, we systematically use several sets of initial parameters in order to obtain a solution which is obviously the latter. Of the 6 fit parameters plus the helicity $H = \pm 1$, four are positive definite: $t_0$, the time of closest approach; $R_0$, the cloud radius; $B_0$, the axial field strength; and $\phi_0$, the azimuth of the cloud axis (while not strictly positive definite, we choose to define it in the range $0° < \phi < 360°$, rather than $-180° < \phi < 180°$). Furthermore, we find that the initial guesses for these these parameters have little effect on the returned solution. Hence, we use the same initial values for them for fitting each cloud: $t_0 = \frac{1}{2}T_{MC}$, $R_0 = 2 \times 10^7$ km, $B_0 = 20$ nT, and $\phi_0 = 135°$.

## Appendix B:

## Comparison of Magnetic Cloud Fits for the Bastille Day 2000 Event

Table 4 shows the fit parameters, current and flux for the Bastille Day 2000 eruption (Event 9 in Tables 1, 2 and 3) for our work and for three other published works [*Lepping et al.*, 2001; *Mulligan et al.*, 2001b; *Lynch et al.*, 2003]. Like our present work, *Lynch et al.* follow Lepping's Lundquist-solution model. *Mulligan et al.*, on the other hand, use a non-force-free cylindrical model.

**Table 4**

The first five rows of Table 4 show the fit parameters $\theta_0$, $\phi_0$, $B_0$, $R_0$ and $Y/R_0$, the normalized impact parameter. The last two rows contain the derived parameters for current and flux, calculated from equations (2) and (3), respectively, for the force-free models. *Mulligan et al.* [2001b] do not quote a value for the current. *Lepping et al.* [2003] recently published uncertainties to their original [*Lepping et al.*, 2001] fit parameters; these are quoted in the relevant column.

We see that there is significant spread in the orientation parameters ($\theta_0$, $\phi_0$ and $Y/R_0$). However, the uncertainties associated with the various models are also quite large. *Lepping et al.* [2003] expect that $Y/R_0$ will usually be the most poorly estimated quantity, as it is here; the Lepping *et al.* fit to the Bastille Day 2000 event has a 1-$\sigma$ uncertainty in $Y/R_0$ of 0.30, or 30%. Given this uncertainly the extreme values of *Lynch et al.* (0.00) and *Mulligan et al.* (0.42) are not significantly different. On the other hand, our value of $\theta_0$ (1°) differs from the (highly inclined) average axis from the other three studies by 3 standard deviations.

There is much less spread in the current and flux values. *Mulligan et al.* [2001b] find values of radius, axial field strength and impact parameter that are all significantly larger than the other models. We attribute this result to the fact that this cloud is particularly well fit by a force-free model. That all clouds are force free is an assumption, but is quite reasonable in low plasma $\beta$ events such as the Bastille Day event ($\langle\beta\rangle < 0.01$). The standard deviation of the total current values in the three force-free models is 12% of the mean, and the standard deviation of the total flux values is 22% of the mean. These uncertainties are small in comparison to those of the current and flux values from the vector magnetograms, and hence are ignored in Figure 3. Further, since current and flux are functions only of $B$ and $R$, the best-constrained fit parameters, and independent of orientation, it is not surprising that there is close agreement between the values of current and flux from three force-free models.

Finally, we note that not all events have such large uncertainties. For instance, in one other event much studied in the literature, the January 1997 event, the average deviation between axis directions between us, *Burlaga et al.* [1998] and *Ruzmaikin et al.* [2003] is

only 14.5°. That event was not included in the present study as it was not associated with a numbered active region.

**Acknowledgments.** Interplanetary *in situ* data were provided by the ISTP-CDAWeb and NSSDC OMNIWeb databases. The online CME catalog is generated and maintained by NASA and The Catholic University of America in cooperation with the Naval Research Laboratory. SOHO is a project of international cooperation between ESA and NASA. Yohkoh is a mission of ISAS in Japan; the SXT instrument is a collaboration of the University of Tokyo, the National Astronomical Observatory of Japan, and the Lockheed Martin Solar and Astrophysics Laboratory.

Funding for this work was provided by AFOSR under grant number F49620-00-1-0128 and the MURI grant to the University of California, Berkeley, and NASA under SR&T grant NAG6-6110. S.L.J. K.L. and B.J.L. participated in this project through the Research Experience for Undergraduates (REU) Program at Montana State University, which is supported by the National Science Foundation under Grant No. 0243923.

## References

Antiochos, S. K., The magnetic topology of solar eruptions, *Astrophys. J.*, *502*, L181–184, 1998.

Antiochos, S. K., C. R. DeVore, and J. A. Klimchuk, A model for solar coronal mass ejections, *Astrophys. J.*, *510*, 485, 1999.

Bothmer, V., and D. M. Rust, The field configuration of magnetic clouds and the solar cycle, in *Coronal Mass Ejections*, edited by N. U. Crooker, J.-A. Joselyn, and J. Feynman, vol. 99 of *Geophysical Monograph Series*, p. 139, American Geophysical Union,

Washington, D.C., 1997.

Bothmer, V., and R. Schwenn, The structure and origin of magnetic clouds in the solar wind, *Ann. Geophys.*, *16*, 1, 1998.

Brueckner, G. E., et al., The Large Angle Spectroscopic Coronagraph (LASCO), *Solar Phys.*, *162*, 357, 1995.

Burlaga, L. F., E. C. Sittler, F. Mariani, and R. Schwenn, Magnetic loop behind an interplanetary shock: Voyager, Helios and IMP8 observations, *J. Geophys. Res.*, *86*, 6673, 1981.

Burlaga, L. F., et al., A magnetic cloud containing prominence material: January 1997, *J. Geophys. Res.*, *103*, 277, 1998.

Burnette, A., R. C. Canfield, and A. A. Pevtsov, Photospheric and coronal currents in solar active regions, *Astrophys. J.*, *in press*, 2004.

Canfield, R. C., J. F. De La Beaujardiere, Y. Fan, K. D. Leka, A. N. McClymont, T. R. Metcalf, D. L. Mickey, J.-P. Wuelser, and B. W. Lites, The morphology of flare phenomena, magnetic fields, and electric currents in active regions. I - Introduction and methods, *Astrophys. J.*, *411*, 362–369, 1993.

Canfield, R. C., H. S. Hudson, and D. E. McKenzie, Sigmoidal morphology and eruptive solar activity, *Geophys. Res. Lett.*, *26*, 627, 1999.

Crooker, N., J. T. Gosling, and S. W. Kahler, Magnetic clouds at sector boundaries, *J. Geophys. Res.*, *103*, 301–306, 1998.

Crooker, N. U., Solar and heliospheric geoeffective disturbances, *J. Atmos. and Solar-Terr. Phys.*, *62*, 1071, 2000.

Delaboudinière, J.-P., et al., EIT: Extreme-Ultraviolet Imaging Telescope for the SOHO Mission, *Solar Phys.*, *162*, 291–312, 1995.

Domingo, V., B. Fleck, and A. I. Poland, The SOHO mission: An overview, *Solar Phys.*, *162*, 1–37, 1995.

Gopalswamy, N., S. Yashiro, G. Michalek, M. L. Kaiser, R. A. Howard, D. V. Reames, R. Leske, and T. von Rosenvinge, Interacting coronal mass ejections and solar energetic particles, *Astrophys. J.*, *572*, L103–L107, 2002.

Gosling, J. T., Coronal mass ejections and magnetic flux ropes in interplanetary space, in *Physics of Magnetic Flux Ropes*, edited by C. T. Russell, E. R. Priest, and L. C. Lee, vol. 58 of *Geophysical Monograph Series*, p. 343, American Geophysical Union, Washington, D.C., 1990.

Howard, R. F., The magnetic fields of active regions. I - Data and first results, *Solar Phys.*, *123*, 271–284, 1989.

Larson, D. E., et al., Tracing the topology of the October 18-20, 1995, magnetic cloud with $\sim 0.1$–$10^2$ keV electrons, *Geophys. Res. Lett.*, *24*, 1911, 1997.

Leamon, R. J., R. C. Canfield, and A. A. Pevtsov, Properties of magnetic clouds and geomagnetic storms associated with eruption of coronal sigmoids, *J. Geophys. Res.*, *107*, 1234, doi:10.1029/2001JA000313, 2002.

Leka, K. D., On the value of $\alpha_{AR}$ from Vector Magnetograph data - II. Spatial Resolution, Field of View, and Validity, *Solar Phys.*, *188*, 21–40, 1999.

Lepping, R. P., and D. B. Berdichevsky, Interplanetary magnetic clouds: Sources, properties, modeling and geomagnetic relationship, *Recent Res. Devel. Geophysics*, *3*, 77, 2000.

Lepping, R. P., J. A. Jones, and L. F. Burlaga, Magnetic field structure of interplanetary magnetic clouds, *J. Geophys. Res.*, *95*, 11 957, 1990.

Lepping, R. P., et al., The WIND magnetic field investigation, *Space Sci. Rev.*, **71**, 207, 1995.

Lepping, R., A. Szabo, C. DeForest, and B. J. Thompson, Magnetic Flux in Modeled Magnetic Clouds at 1 AU and Some Specific Comparisons to Associated Photospheric flux, in *Proc. 31st ESLAB Symposium, "Correlated Phenomena at the Sun, in the Heliosphere, and in Geospace", ESTEC, Noordwijk, The Netherlands, 22-25 September 1997 (ESA SP-415)*, pp. 163–170, 1997.

Lepping, R. P., et al., The Bastille Day magnetic clouds and upstream shocks: Near-Earth interplanetary observations, *Solar Phys.*, *204*, 287, 2001.

Lepping, R. P., D. B. Berdichevsky, and T. J. Ferguson, Estimated errors in magnetic cloud model fit parameters with force-free cylindrically symmetric assumptions, *J. Geophys. Res.*, *108*, 1356, doi:10.1029/2002JA009657, 2003.

Luhmann, J. G., Y. Li, C. Arge, X.-P. Zhao, Y. Liu, O. C. St. Cyr, and N. Rich, Using potential field models to learn about CME coronal context and consequences, *American Astronomical Society Meeting*, *200*, 2002.

Lundquist, S., Magnetohydrostatic fields, *Ark. Fys.*, **2**, 361, 1950.

Lynch, B. J., P. J. MacNeice, S. K. Antiochos, T. H. Zurbuchen, and L. A. Fisk, Breakout model 'realism': A comparison to observations, *Banff SHINE Meeting*, 2002.

Lynch, B. J., T. H. Zurbuchen, L. A. Fisk, and S. K. Antiochos, Internal structure of magnetic clouds: Plasma and composition, *J. Geophys. Res.*, *108*, 1239, doi:10.1029/2002JA009591, 2003.

Mickey, D. L., The Haleakala Stokes Polarimeter, *Solar Phys.*, *97*, 223–238, 1985.

Mulligan, T., C. T. Russell, and J. G. Luhmann, Solar cycle evolution of the structure of magnetic clouds in the inner heliosphere, *Geophys. Res. Lett.*, *25*, 2959, 1998.

Mulligan, T., C. T. Russell, and J. G. Luhmann, Interplanetary magnetic clouds: Statistical patterns and radial variations, *Adv. Space Res.*, *26*, 801–806, 2000.

Mulligan, T., C. T. Russell, B. J. Anderson, and M. H. Acuña, Multiple spacecraft flux rope modeling of the Bastille Day magnetic cloud, *Geophys. Res. Lett.*, *28*, 4417, 2001b.

Nelder, J. A., and R. Mead, A simplex method for function minimisation, *Computer J.*, **7**, 308, 1965.

Ogilvie, K. W., et al., SWE, a comprehensive plasma instrument for the WIND spacecraft, *Space Sci. Rev.*, **71**, 55, 1995.

Pevtsov, A. A., and R. C. Canfield, Solar magnetic fields and geomagnetic events, *J. Geophys. Res.*, *106*, 25 191–25 197, 2001.

Pevtsov, A. A., R. C. Canfield, and T. R. Metcalf, Latitudinal variation of helicity of photospheric magnetic fields, *Astrophys. J. Lett.*, *440*, 109, 1995.

Press, W. H., S. A. Teukolsky, W. T. Vetterling, and B. P. Flannery, *Numerical Recipes in FORTRAN 77*, 2nd ed., Cambridge Univ. Press, New York, 1992.

Ruzmaikin, A., S. Martin, and Q. Hu, Signs of magnetic helicity in interplanetary mass ejections and associated prominences, *J. Geophys. Res.*, *108*, 1096, doi:10.1029/2002JA009588, 2003.

Scherrer, P. H., et al., The Solar Oscillations Investigation - Michelson Doppler Imager, *Solar Phys.*, *162*, 129–188, 1995.

Skumanich, A., and B. W. Lites, Stokes profile analysis and vector magnetic fields. i - inversion of photospheric lines, *Astrophys. J.*, *322*, 473–482, 1987.

Subramanian, P., and K. P. Dere, Source regions of coronal mass ejections, *Astrophys. J.*, *561*, 372–395, 2001.

Titov, V. S., and P. Démoulin, Basic topology of twisted magnetic configurations in solar flares, *Astron. Astrophys.*, *351*, 707, 1999.

Tsuneta, S., et al., The Soft X-ray Telescope for the SOLAR-A mission, *Solar Phys.*, *136*, 37–67, 1991.

Webb, D. F., Coronal mass ejections: Origins, evolution and role in space weather, *IEEE Trans. Plasma Sci.*, *28*, 1795, 2000.

Webb, D. F., R. P. Lepping, L. F. Burlaga, C. E. DeForest, D. E. Larson, S. F. Martin, S. P. Plunkett, and D. M. Rust, The origin and development of the May 1997 magnetic cloud, *J. Geophys. Res.*, *105*, 27 251, 2000b.

Zhang, M., and B. C. Low, Magnetic flux emergence into the solar corona. III. The role of magnetic helicity conservation, *Astrophys. J.*, *584*, 479, 2003.

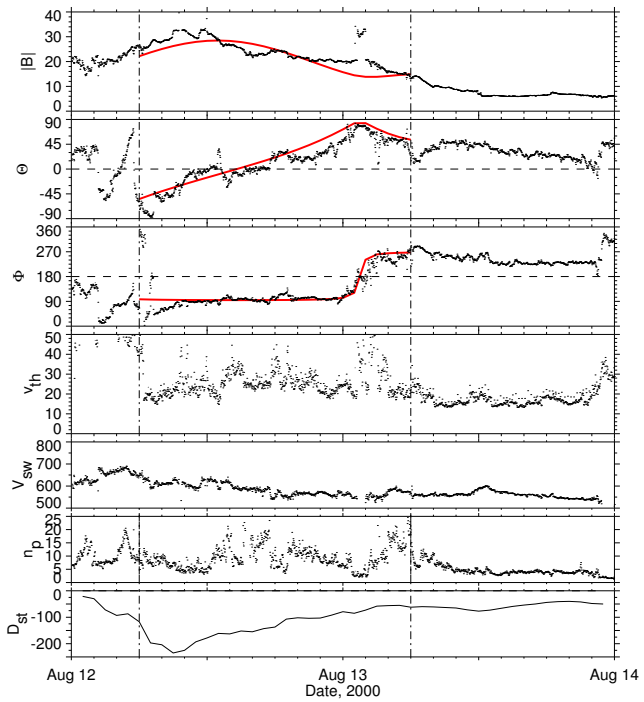


**Figure 1.** Summary plot of cloud event No. 12, showing a model fit of typical quality ($\chi^2/B_0^2 = 0.024$) to magnetic field magnitude ($|B|$), direction ($\Theta$, $\Phi$) and the constant-$\alpha$ force-free field fit (smooth curves). The lower 4 panels are, respectively, proton thermal speed, radial solar wind component, proton density and $D_{st}$ geomagnetic storm index. *In situ* data as observed by Wind at 1 AU. Vertical dashed lines delineate the cloud boundaries.

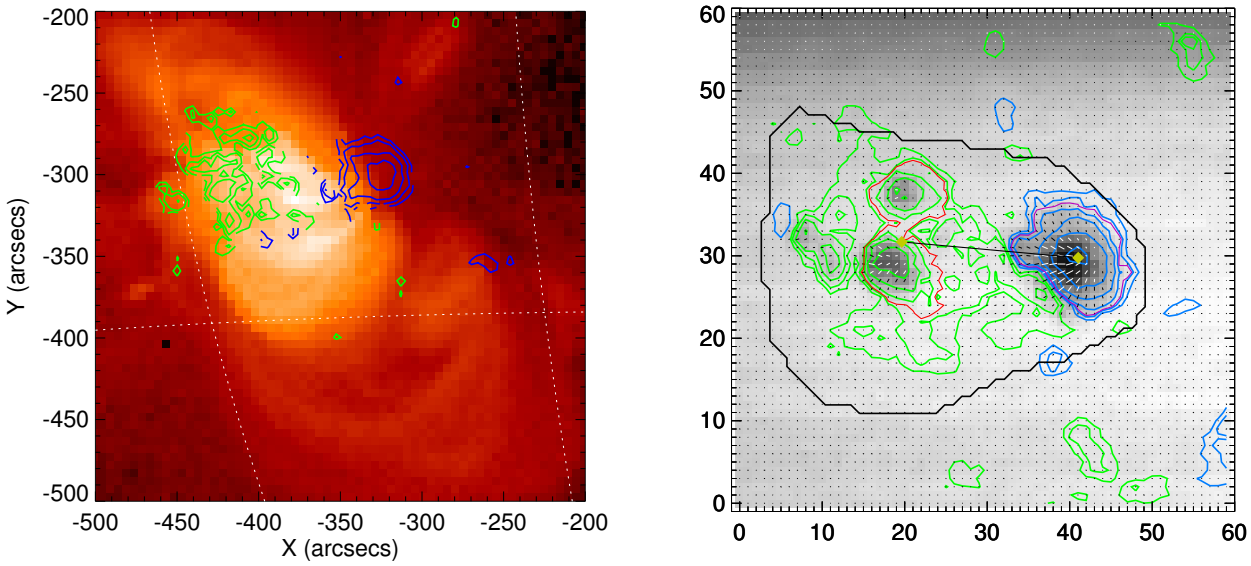


**Figure 2.** Sample Yohkoh SXT Al.1 image and MDI magnetogram overlay (left panel) and annotated HSP vector magnetogram (right panel) for the analysis of event No. 4. Left panel: Green/blue contours—positive/negative magnetic flux. Solar North up, West right; X and Y relative to disk center, units seconds of arc. Right panel: Green/blue contours—positive/negative magnetic flux. Red/purple contours—boundaries for the calculation of centers of flux and $\ell$. Black contour: boundary for calculation of $J_z$. Earth North up, West right; scan row and column numbers in units of magnetogram pixels (2.83″).

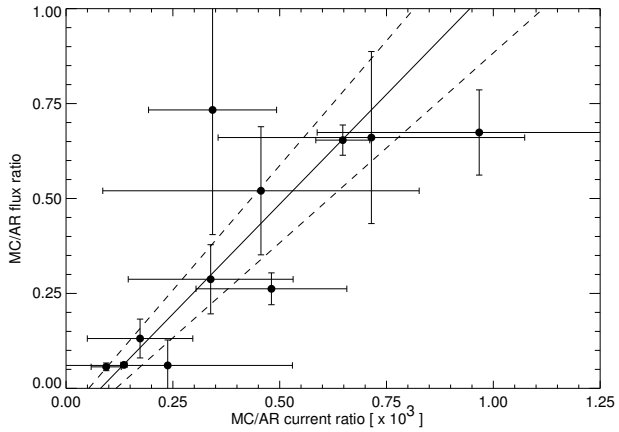


**Figure 3.** Flux ratio versus current ratio. The lower and upper ends of the ordinate error bars are $\Phi_{AR}^{300}$ and $\Phi_{AR}$, respectively, and the plotted bullet is their mean; similarly the abscissa data points and error bars are from $I_{AR}^{300}$ and $I_{AR}$. Following Appendix B, we ignore the smaller uncertainty of MC current and flux values.

**Table 1.** Magnetic cloud events—fit parameters and inferred quantities.

| No. | Year | Cloud Times: Start | End | $\theta_0$ (deg) | $\phi_0$ (deg) | $B_0$ (nT) | $R_0$ (Gm) | H | $\chi^2/B_0^2$ | $I_{MC}$ (GA) | $\Phi_{MC}$ (TWb) | $\alpha_{MC}$ ($Gm^{-1}$) |
|---|---|---|---|---|---|---|---|---|---|---|---|---|
| 1 | 1995 | Feb 08 03h | Feb 08 22h | −18 | 81 | 12.7 | 16.6 | − | 0.016 | 0.55 | 4.74 | 0.15 |
| 2 | – | Mar 04 11h | Mar 05 04h | −55 | 154 | 11.8 | 14.2 | − | 0.035 | 0.44 | 3.26 | 0.17 |
| 3 | – | Dec 16 05h | Dec 16 22h | 39 | 50 | 11.6 | 34.2 | − | 0.023 | 1.03 | 18.5 | 0.07 |
| 4 | 1998 | Feb 17 10h | Feb 18 18h | −5 | 310 | 17.6 | 19.0 | + | 0.032 | 0.87 | 8.69 | 0.13 |
| 5 | – | May 02 12h | May 03 17h | −9 | 357 | 10.5 | 33.6 | + | 0.035 | 0.91 | 16.0 | 0.07 |
| 6 | 1999 | Feb 18 14h | Feb 19 12h | 41 | 58 | 16.8 | 35.4 | − | 0.011 | 1.54 | 28.6 | 0.07 |
| 7 | – | Aug 09 10h | Aug 10 16h | 59 | 270 | 12.8 | 23.5 | − | 0.023 | 0.78 | 9.59 | 0.10 |
| 8 | – | Sep 21 21h | Sep 22 05h | 6 | 90 | 14.7 | 7.08 | − | 0.011 | 0.27 | 0.99 | 0.34 |
| 9 | 2000 | Jul 15 19h | Jul 16 09h | 1 | 62 | 48.1 | 26.4 | − | 0.015 | 3.29 | 45.5 | 0.09 |
| 10 | – | Jul 28 21h | Jul 29 11h | 5 | 319 | 14.6 | 16.4 | − | 0.026 | 0.62 | 5.33 | 0.15 |
| 11 | – | Aug 01 00h | Aug 01 16h | 18 | 118 | 12.3 | 40.9 | − | 0.012 | 1.31 | 27.9 | 0.06 |
| 12 | – | Aug 12 06h | Aug 13 05h | −11 | 82 | 29.1 | 25.1 | + | 0.024 | 1.90 | 24.9 | 0.10 |

**Table 2.** Solar observations and inferred quantities.

| No. | Year | Event Times: Eruption | Magnetogram | AR | $I_{AR}$ (TA) | $\Phi_{AR}$ (TWb) | $\ell$ (Mm) | $\alpha_{AR}$ ($Gm^{-1}$) | AR Tilt (°) |
|---|---|---|---|---|---|---|---|---|---|
| 1 | 1995 | Feb 04 15:56 | Feb 04 01:51 | 7834 | 0.97–2.28 | 12.8–20.2 | 42.2 | −5.1 | −30 |
| 2 | – | Feb 28 08:46 | Feb 27 17:17 | 7846 | 1.26–3.82 | 18.0–31.7 | 40.7 | −0.7 | 45 |
| – | – | – | Feb 28 19:45 | – | 1.91–3.39 | 29.2–39.4 | 61.3 | −9.4 | −6 |
| 3 | – | Dec 11 03:31 | Dec 10 17:22 | 7930 | 0.63–2.36 | 6.64–12.1 | 35.5 | 34.8 | −17 |
| – | – | – | Dec 11 17:15 | – | 0.48–1.56 | 7.25–13.8 | 34.0 | 24.4 | −33 |
| 4 | 1998 | Feb 14 02:29 | Feb 12 17:33 | 8156 | 1.34–2.28 | 29.4–36.9 | 44.1 | −12.3 | −5 |
| 5 | – | Apr 29 16:58† | Apr 28 16:38 | 8210 | 0.85–3.14 | 23.7–37.8 | 60.7 | 17.2 | 79 |
| – | – | – | Apr 29 16:39 | – | 1.02–2.25 | 24.7–37.1 | 29.9 | 27.0 | −20 |
| 6 | 1999 | Feb 14 11:16 | Feb 11 19:26 | 8457 | 1.39–2.92 | 32.8–53.8 | 62.3 | −4.7 | 29 |
| 7 | – | Aug 04 04:11 | Aug 02 16:36 | 8651 | 6.10–10.5 | 148.0–191.0 | 90.2 | −7.5 | −29 |
| 8 | – | Sep 17 22:28 | Sep 20 17:00 | 8700 | 0.15–2.12 | 3.51–29.3 | 70.1 | −5.4 | −15 |
| 9 | 2000 | Jul 14 09:27 | Jul 11 16:52 | 9077 | 4.73–5.43 | 66.5–72.6 | 102.5 | −48.4 | 0 |
| – | – | – | Jul 14 16:39 | – | 5.03–5.79 | 47.6–80.4 | 65.6 | −52.9 | 10 |
| – | – | – | Jul 17 16:32 | – | 0.73–1.66 | 19.0–30.6 | 34.9 | −29.2 | −75 |
| 10 | – | Jul 25 02:48 | Jul 21 20:28 | 9097 | 4.40–4.75 | 84.3–88.4 | 57.8 | −15.6 | 17 |
| 11 | – | Jul 27 22:18 | Jul 26 16:33 | 9097 | 2.64–5.00 | 26.0–50.1 | 53.3 | 16.9 | 29 |
| – | – | – | Jul 28 16:40 | – | 0.51–1.39 | 10.9–21.0 | 41.4 | −17.5 | 63 |
| 12 | – | Aug 09 16:30† | Aug 08 16:37 | 9114 | 1.42–2.51 | 32.6–41.3 | 85.3 | −12.7 | −17 |
| – | – | – | Aug 11 16:58 | – | 1.88–2.94 | 42.1–52.4 | 77.9 | −9.8 | 83 |

† Time from SoHO/LASCO; gap in Yohkoh temporal coverage.

**Table 3.** Comparison of flux, current, and twist values in ARs and MCs.

| No. | Year | Event Times: Eruption | Event Times: Magnetogram | AR | $I_{MC}/I_{AR}$ $\times 10^{-3}$ | $\Phi_{MC}/\Phi_{AR}$ % | $(\alpha L)_{AR}$ | $(\alpha L)_{MC}$‡ |
|---|---|---|---|---|---|---|---|---|
| 1 | 1995 | Feb 04 15:56 | Feb 04 01:51 | 7834 | 0.15–0.53 | 20–38 | −0.34 | −53.2 |
| 2 | – | Feb 28 08:46 | Feb 27 07:17 | 7846 | 0.05–0.30 | 8–18 | −0.01 | −62.2 |
| – | – | – | Feb 28 19:45 | – | 0.12–0.28 | 8–12 | −0.91 | – |
| 3 | – | Dec 11 03:31 | Dec 10 17:22 | 7930 | 0.13–1.25 | 115–279 | 1.94 | −25.8 |
| – | – | – | Dec 11 17:15 | – | 0.58–4.02 | 122–314 | 1.30 | – |
| 4 | 1998 | Feb 14 02:29 | Feb 12 17:33 | 8156 | 0.30–0.66 | 22-30 | −0.85 | +43.1 |
| 5 | – | Apr 29 16:58 | Apr 28 16:38 | 8210 | 0.09–0.83 | 35–69 | 1.64 | +26.3 |
| – | – | – | Apr 29 16:39 | – | 0.36–1.19 | 40–72 | 1.27 | – |
| 6 | 1999 | Feb 14 11:16 | Feb 11 19:26 | 8457 | 0.36–1.07 | 43–89 | −0.46 | −25.0 |
| 7 | – | Aug 04 04:11 | Aug 02 16:36 | 8651 | 0.06–0.13 | 5–7 | −1.06 | −37.6 |
| 8 | – | Sep 17 22:28 | Sep 20 17:00 | 8700 | 0–0.53 | 0–13 | −0.59 | −124.8 |
| 9 | 2000 | Jul 14 09:27 | Jul 11 16:52 | 9077 | 0.58–0.71 | 61–69 | −7.79 | −33.5 |
| – | – | – | Jul 14 16:39 | – | 0.55–0.68 | 52–112 | −5.45 | – |
| – | – | – | Jul 17 16:32 | – | 1.78–6.12 | 138–274 | −1.60 | – |
| 10 | – | Jul 25 02:48 | Jul 21 20:28 | 9097 | 0.13–0.14 | 6.0–6.4 | −1.42 | −53.9 |
| 11 | – | Jul 27 22:18 | Jul 26 16:33 | 9097 | 0.19–0.49 | 40–106 | 1.42 | −21.6 |
| – | – | – | Jul 28 16:40 | – | 0.83–4.00 | 121–317 | −1.14 | – |
| 12 | – | Aug 09 16:30 | Aug 08 16:37 | 9114 | 0.59–1.35 | 56–79 | −1.70 | +35.2 |
| – | – | – | Aug 11 16:58 | – | 0.60–1.14 | 46–62 | −1.19 | – |

‡ Assuming $L = 2.5$ AU.

**Table 4.** Comparison of fit parameters: Bastille Day 2000 event.

| Fit Parameter | | Present Work | *Lepping et al.* [2001, 2003] | *Lynch et al.* [2003] | *Mulligan et al.* [2001b] |
|---|---|---|---|---|---|
| $\theta_0$ | [deg] | 1 | 55±13 | 28 | 40 |
| $\phi_0$ | [deg] | 62 | 46±32 | 64 | 83 |
| $B_0$ | [nT] | 48.1 | 46.8±3.3 | 44.3 | 77 |
| $R_0$ | [$10^6$ km] | 26.4 | 27.8±1.6 | 23.5 | 35.3 |
| $Y/R_0$ | | 0.09 | 0.16±0.30 | 0.00 | 0.42 |
| $I_{MC}$ | [$10^9$ A] | 3.3 | 3.4 | 2.7 | – |
| $\Phi_{MC}$ | [$10^{12}$ Wb] | 46 | 52 | 33 | 95 |